mater.scichina.com link.springer.com

Published online 26 January 2021 | https://doi.org/10.1007/s40843-020-1567-2
Sci China Mater 2021, 64(7): 1621–1631

Tailored Sr-Co-free perovskite oxide as an air electrode for high-performance reversible solid oxide cells

Wenjie Wang[1], Yunfeng Tian[1*], Yun Liu[2], Nalluri Abhishek[1], Yitong Li[1], Bo Chi[1,3*] and Jian Pu[1,3]

ABSTRACT **Sr-Co containing perovskite oxides are prospective air electrode candidates for reversible solid oxide cells (RSOCs). However, their efficiencies are limited by Sr segregation and the high thermal expansion coefficient (TEC) of Co-based perovskites. Herein, $La_{0.6}Ca_{0.4}Fe_{0.8}Ni_{0.2}O_{3-\delta}$ (LCaFN) is tailored as an Sr-Co-free perovskite air electrode for high-performance RSOCs. Compared with $La_{0.6}Sr_{0.4}Fe_{0.8}Ni_{0.2}O_{3-\delta}$ (LSFN) and $La_{0.6}Sr_{0.4}Co_{0.2}Fe_{0.8}O_{3-\delta}$ (LSCoF), LCaFN has a high electrical conductivity (297 S cm^{-1}), TEC compatibility (11.2 × 10^{-6} K^{-1}) and improved chemical stability. Moreover, LCaFN has high oxygen reduction reaction (ORR) activity with a low polarization resistance (0.06 Ω cm^2) at 800°C. A single-cell Ni-YSZ/YSZ/gadolinium-doped ceria (GDC)/LCaFN-GDC operated at 800°C yields a maximum power density of 1.08 W cm^{-2} using H_2 as fuel. In the solid oxide electrolysis cell (SOEC) mode, the cell can achieve a current density of approximately 1.2 A cm^{-2} at 1.3 V with 70% humidity at 800°C. The cell exhibits good reversibility and remains stable in continuous SOEC and solid oxide fuel cell (SOFC) modes. These findings indicate the potential application of LCaFN as an air electrode material for RSOCs.**

Keywords: reversible solid oxide cell, Sr-Co-free, composite oxide, hydrogen production, reversibility

INTRODUCTION

Reversible solid oxide cells (RSOCs) are green and efficient electrochemical energy conversion solid-state devices. They can be used as solid oxide fuel cells (SOFCs) to convert the chemical energy of fuel into electrical energy without burning and also as solid oxide electrolysis cells (SOECs) to convert excess electrical energy into chemical energy [1–3]. Therefore, RSOCs are anticipated to be prominently utilized for large-scale energy storage [4,5]. A typical RSOC is a three-component system, comprising an electrolyte such as yttria-stabilized zirconia (YSZ), a fuel electrode (Ni-YSZ), and an air electrode $La_{0.8}Sr_{0.2}MnO_3$ (LSM) [6]. The performance of RSOCs significantly relies on the air electrode. It is responsible for conducting the oxygen reduction reaction (ORR) and oxygen evolution reaction (OER) during the discharging and charging processes, respectively [7–9]. Thus, it is crucial to develop a reliable air electrode with high electrocatalytic activity for RSOCs.

Perovskite oxides of various compositions have been engineered and studied as air electrodes. Among them, cobalt-based perovskite oxides have attracted much attention due to their excellent electrocatalytic activity and outstanding electrical conductivity. A high current density of 0.95 A cm^{-2} was obtained by impregnating $La_{0.8}Sr_{0.2}Co_{0.8}Ni_{0.2}O_{3-\delta}$ into the gadolinium-doped ceria (GDC) framework as the SOEC air electrode at 750°C and 1.3 V [10]. López-Robledo *et al.* [11] used $La_{0.6}Sr_{0.4}Co_{0.2}Fe_{0.8}O_{3-\delta}$ (LSCoF) as an air electrode for microtube cells and obtained a power density of 695 mW cm^{-2} at 0.7 V and 800°C and a current density of 0.845 A cm^{-2} at 1.3 V. Other electrode materials have also been investigated, such as $La_{0.5}Sr_{0.5}Co_{0.8}Cu_{0.2}O_{3-\delta}$ [12], $Ba_{0.5}Sr_{0.5}Co_{0.8}Fe_{0.2}O_{3-\delta}$ [13] and $PrBaCo_2O_{5+\delta}$ [14]. However, due to the mismatched thermal expansion coefficient (TEC) between the cobalt-based oxide and YSZ electrolyte, the electrode and electrolyte will crack or separate during long-term

[1] Center for Fuel Cell Innovation, School of Materials Science and Engineering, Huazhong University of Science and Technology, Wuhan 430074, China
[2] China-EU Institute for Clean and Renewable Energy, Huazhong University of Science and Technology, Wuhan 430074, China
[3] Key Laboratory of Material Chemistry for Energy Conversion and Storage of Ministry of Education, Huazhong University of Science and Technology, Wuhan 430074, China
* Corresponding authors (emails: yunfengup@163.com (Tian Y); chibo@hust.edu.cn (Chi B))

thermal cycling, thereby disrupting the mass transfer and charge exchange processes. Moreover, reversible SOFC/SOEC operation modes further deteriorate the air electrode-electrolyte interface [15,16]. Other demerits include the high cost of cobalt-based perovskites and accelerated cobalt volatilization during high-temperature sintering [17,18]. Therefore, the development of cobalt-free air electrodes is expected.

Compared with the cobalt-based perovskite oxide, the nickel-iron-based mixed ion-electron conductor (MIEC) perovskite oxide has better compatibility with YSZ electrolyte TEC and higher ORR catalytic activity [18–20]. In our previous research, we found that $La_{0.6}Sr_{0.4}Fe_{0.8}Ni_{0.2}O_{3-\delta}$ (LSFN) showed good ORR and OER performances [21]. RSOCs with LSFN as the air electrode achieved a peak power density of 961 mW cm^{-2} at 800°C (SOFC mode) and a current density of 1.09 A cm^{-2} at 850°C under 1.3 V (SOEC mode). Sr-containing perovskite oxide has good electrocatalytic activity. However, the surface segregation of Sr-based oxides during long-term operation is severe, which destabilizes the structure and composition of the perovskite oxides, and further harms the catalytic activity of the electrode. For example, the formation and segregation of $SrZrO_3$ at the electrolyte-air electrode interface can be observed during prolonged high-temperature operation [22,23]. Moreover, Sr^{2+} has a high affinity to react with Cr-rich stainless steel components to produce deleterious reactants, namely $SrCrO_4$ (Cr poisoning), during SOFC operation [24,25]. Therefore, the use of Sr-free perovskite oxides is desirable for SOFC applications.

Sr-Co-free $La_{0.6}Ca_{0.4}Fe_{0.8}Ni_{0.2}O_{3-\delta}$ (LCaFN) perovskite oxide is investigated in this study. The physicochemical properties and electrochemical performance of LCaFN are studied and compared with those of LSCoF and LSFN. The electrochemical performance of RSOCs with an LCaFN air electrode is evaluated in detail. The results show that LCaFN has high electrocatalytic activity and can achieve excellent performance in both SOFC and SOEC modes. Therefore, LCaFN is a promising air electrode for RSOCs.

EXPERIMENTAL SECTION

Material synthesis and cell fabrication

The LCaFN powders were prepared by a sol-gel method [21]. $La(NO_3)_3{\cdot}6H_2O$ (Aladdin 99%), $Ca(NO_3)_2{\cdot}4H_2O$ (Aladdin 99%), $Fe(NO_3)_3{\cdot}9H_2O$ (Aladdin 99%) and $Ni(NO_3)_2{\cdot}6H_2O$ (Aladdin 99%) were used as chemical precursors. First, the stoichiometric chemical precursors, citric acid (CA) and ethylenediaminetetraacetic acid (EDTA) were dissolved in distilled water according to the molar ratio of metal ions (Me):EDTA:CA = 1:1:1.5. After complete dissolution, ammonia hydroxide was added to the solution to adjust the pH to 8. With heating and continuous stirring at 80°C, the solution thickened to form a stable gel. The gel was then dried in an oven at 200°C to obtain the precursor. Finally, the precursor was calcined in air at 800°C (5°C min^{-1}) for 5 h to obtain LCaFN powders. LSFN powders were also synthesized separately by the same method.

A half-cell was designed to study the OER and ORR activities of LCaFN [26]. For the single cell, the Ni-YSZ support with a weight ratio of 57:43 was prepared by the tape casting method. Ni-YSZ (60:40, wt%) fuel electrode and YSZ electrolyte paste were coated on the support by the screen-printing method, and then cosintered at 1390°C for 4 h. A thin GDC barrier layer was coated onto the YSZ electrolyte, followed by sintering at 1300°C for 5 h. Finally, the screen-printed LCaFN-GDC composite (60:40, wt%) was calcined at 1000°C for 2 h to form a single cell. The active cell area was 0.5 cm^2, and Pt was employed as the current collector.

Characterization and electrochemical test

The crystal structure of LCaFN was determined by powder X-ray diffraction (XRD) analysis (Cu Kα, 40 kV, 40 mA, Shimadzu XRD-7000S, Japan) and the Rietveld refinement method with GSAS/EXPGUI software. The microstructure of the powders was characterized by transmission electron microscopy (TEM, JEOL JEM-2011, Japan). The morphology of the cell cross-section was observed with a scanning electron microscope (SEM, Sirion 200). For electrical conductivity measurements, LCaFN powders were pressed into a bar of 24 mm × 6 mm × 2 mm, calcined at 1350°C and then measured by the four-point probe method. The TEC of LCaFN was tested by a thermal dilatometer (NETZSCH DIL402C, Germany). The stability of LCaFN was studied using the hydrogen-programmed reduction (H_2-TPR) method. The gas flow rate was maintained at 30 mL min^{-1}. The powders were pretreated in Ar at 350°C for 1 h, and then heated from 20 to 950°C in a 5% H_2/N_2 atmosphere for the H_2-TPR test (heating rate of 10°C min^{-1}). A thermogravimetric analyzer (TGA, STA449F5, NETZSCH, Germany) was used to measure the mass change of the powders from 20 to 1000°C in air.

The fabricated cell was positioned in a tube furnace and sealed with a high-temperature ceramic adhesive (552-VFG, Aremco) for single-cell testing. In the SOFC mode, wet H_2 (3% H_2O) was pumped to the fuel electrode at

100 mL min^{-1} and air was fed to the air electrode at the same flow rate. In the SOEC mode, the water content was controlled by monitoring the temperature of the thermostatic water bath. A powerful electrochemical workstation (a Zennium IM6 station) was deployed for electrochemical performance testing, including the current density-voltage curve, electrochemical impedance spectroscopy, and reversibility and stability tests. The data were measured in a temperature range of 650–850°C with an interval step of 50°C. The frequency range for impedance data recording was from 0.1 Hz to 100 kHz with an amplitude of 10 mV.

RESULTS AND DISCUSSION

Material characterization

Fig. 1a shows the crystal structure of the LCaFN powders. The patterns matched the characteristic peaks of the perovskite structure well, implying the high purity of the synthesized powders. LCaFN has a symmetrical cubic perovskite structure ($Pm\bar{3}m$ space group). The unit cell parameters and volumes of the three samples (LSCoF, LSFN, and LCaFN) are listed in Table 1.

Compared with LSCoF and LSFN (Fig. S1), LCaFN possesses smaller lattice constants due to the smaller ionic radii of Ca^{2+} (1.12 Å) and Ni^{2+} (0.69 Å) compared with Sr^{2+} (1.18 Å) and Co^{2+} (0.745 Å). Furthermore, Ca doping will be more suitable than Sr doping because of the smaller ionic radius of Ca^{2+} compared with Sr^{2+}. The morphology of LCaFN powders is shown in Fig. 1b, which displays a network-like distribution of fine particles with a size of 200 nm. The fine particles of LCaFN were further confirmed by TEM as shown in Fig. 1c. In addition, the elemental chemical composition is in

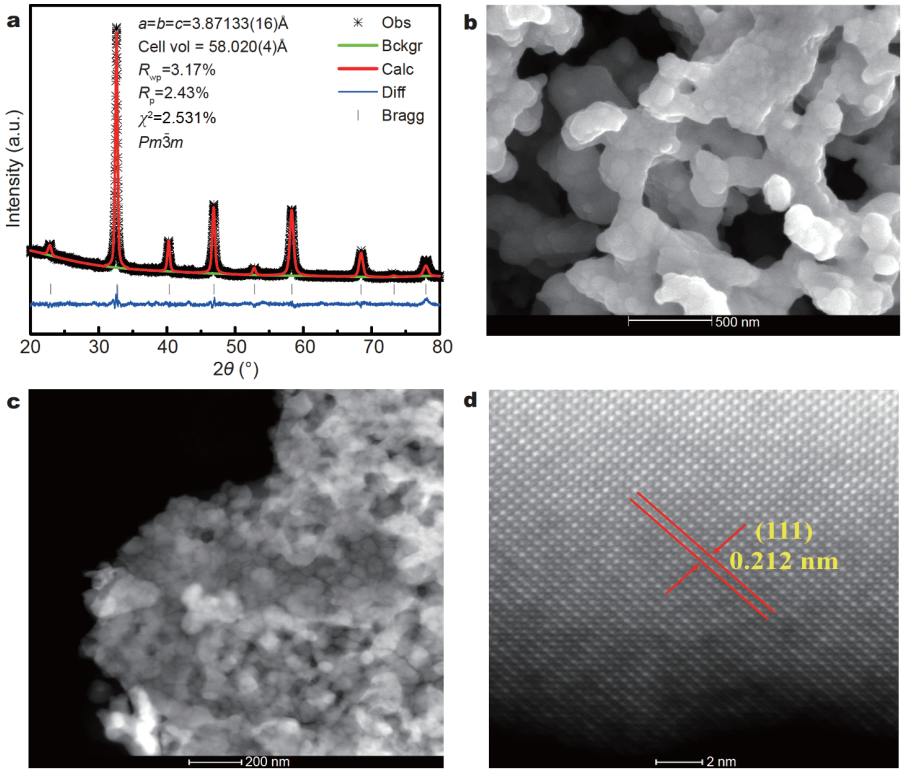

Figure 1 (a) Rietveld refinement of XRD patterns. (b) SEM, (c) TEM and (d) high-resolution TEM images of LCaFN powders.

Table 1 Comparison of the lattice parameters of LSFN, LCaFN and LSCoF

Samples	a (Å)	b (Å)	c (Å)	V (Å^3)	Space Group
$La_{0.6}Ca_{0.4}Fe_{0.8}Ni_{0.2}O_{3-\delta}$	3.871	3.871	3.871	58.02	$Pm\bar{3}m$
$La_{0.6}Sr_{0.4}Fe_{0.8}Ni_{0.2}O_{3-\delta}$ [26]	3.894	3.894	3.894	59.028	$Pm\bar{3}m$
$La_{0.6}Sr_{0.4}Fe_{0.8}Co_{0.2}O_{3-\delta}$ [27]	3.886	3.886	3.886	58.873	$Pm\bar{3}m$

agreement with the theoretical stoichiometric ratio (Fig. S2) while having a homogeneous distribution of the elements (Fig. S3). Moreover, Fig. 1d shows an HR-TEM image of LCaFN powders. The lattice fringe spacing is 0.212 nm, corresponding to the (111) plane of cubic perovskite LCaFN.

Fig. 2a shows the electrical conductivities (σ) of LSFN, LCaFN and LSCoF in air over a temperature range of 100–900°C. The electronic conductivities of the three samples increase first and then decrease with temperature after reaching the maximum value. This phenomenon reflects the small polaron conduction (i.e., localized electronic carriers having a thermally activated mobility) and objects to the Zener double exchange process [28]. The maximum electronic conductivity of LCaFN is 297 S cm^{-1}, which is higher than that of LSFN (130 S cm^{-1}) and slightly lower than that of LSCoF (314 S cm^{-1}). This is attributed to the fact that the electronegativity difference between Co^{3+} and O^{2-} is smaller than that between Fe^{3+} and O^{2-}, so the covalent Co–O bonds are stronger than the Fe–O bonds [29,30]. Increasing the content of Co^{3+} will contribute to enhancing the degree of overlap between the M 3d and O 2p orbitals and promoting electron migration, which will increase the electrical conductivity of LSCoF. Fig. 2b demonstrates the TEC results of LCaFN and LSFN in air. The TECs of LCaFN and LSFN are 11.2 × 10^{-6} and 11.9 × 10^{-6} K^{-1}, respectively, which are lower than that of LSCoF (19.95 × 10^{-6} K^{-1} at 100–800°C) [31]. It should be noted that these values match well with the TEC of GDC (12 × 10^{-6} K^{-1}) [32], which will enhance the adhesion strength with the GDC buffer layer and increase the thermomechanical interface stability. Fig. 2c displays H_2-TPR curves of LSFN and LCaFN. It is observed that there are basically two reduction peaks in the temperature range of 100–900°C. The reduction peak α at around 400°C indicates the transformation of Ni^{3+} to Ni^{2+}, while the second peak β indicates the further reduction of Ni^{2+} to Ni^0 together with a slight reduction from Fe^{3+} to Fe^{2+} [33–35]. Compared with the TPR curves of LSFN and LSCoF [36], it can be seen that the reduction temperature corresponding to the second characteristic peak of LCaFN is much higher than that of LSFN, which further proves that the structure of LCaFN is more stable than that of LSFN and

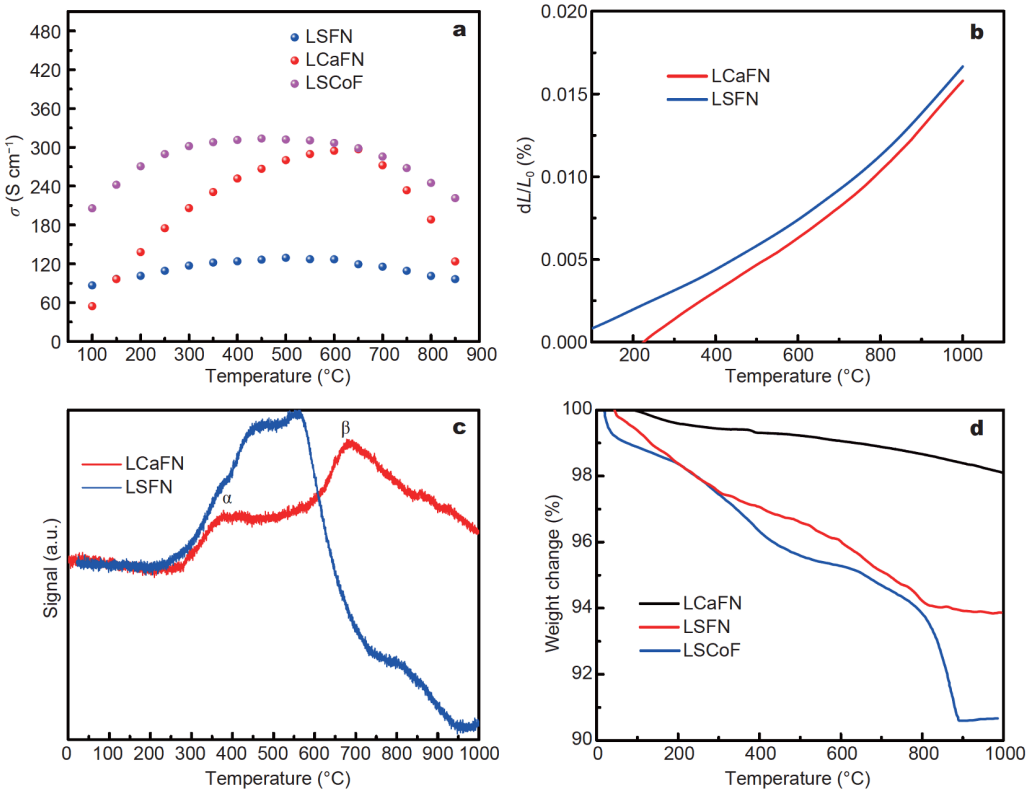

Figure 2 (a) The electronic conductivities *versus* temperature of three samples. (b) TEC of LCaFN and LSFN. (c) H_2-TPR profiles of LCaFN and LSFN. (d) TG curves of LCaFN, LSFN and LSCoF.

LSCoF. This can also be confirmed by the TG curves of the three samples in air from 100 to 900°C, as shown in Fig. 2d. The calculated weight loss of LCaFN is just 1.8%. However, under the same conditions, the weight loss of LSFN and LSCoF can reach 6.2% and 9.58%, respectively. These results suggest that LCaFN exhibits good structural stability.

Electrochemical performance

Half-cell performance

Fig. 3a shows the LCaFN electrode's polarization resistance (R_p) in air at different temperatures. The R_p values of LCaFN are 0.14, 0.06 and 0.03 Ω cm^2 at 750, 800 and 850°C, respectively, which are much lower than those of LSFN (0.5, 0.21 and 0.1 Ω cm^2) [26] and LSCoF (0.672, 0.367 and 0.225 Ω cm^2) [37]. R_p decreases with temperature, indicating a thermal activation behavior in the ORR. Moreover, the ORR (cathodic polarization) and OER (anodic polarization) performance of the LCaFN electrode are characterized by different polarization current densities. Fig. 3b shows the ORR performance of the LCaFN electrode. At current densities of 0 to −500 mA cm^{-2}, the R_p values of the half-cell are 0.112, 0.07, 0.126, 0.13, 0.131 and 0.103 Ω cm^2. It can be observed that the R_p of LCaFN first decreases with increasing polarization current, increases to reach equilibrium and then begins to descend. However, for OER performance, the R_p of LCaFN increases first and then decreases, as shown in Fig. 3c and Fig. S4. This phenomenon indicates that, under different applied currents, the LCaFN electrode undergoes a different electrical activation process. Small R_p values and overpotentials (Fig. S5) further imply that LCaFN has good electrocatalytic activity in both the ORR and OER modes. Fig. 3d shows the electrochemical impedance spectroscopy (EIS) of the LCaFN electrode at open circuit voltage (OCV), 0.5 and −0.5 A cm^{-2}; the R_p values are 0.126, 0.134 and 0.117 Ω cm^2, respectively. A similar value indicates that the LCaFN electrode exhibits good reversibility. Moreover, it can also be seen that the LCaFN electrode has a lower R_p value in ORR mode, indicating that it has better ORR catalytic performance. A comparison of the R_p and activation energy of three electrodes at

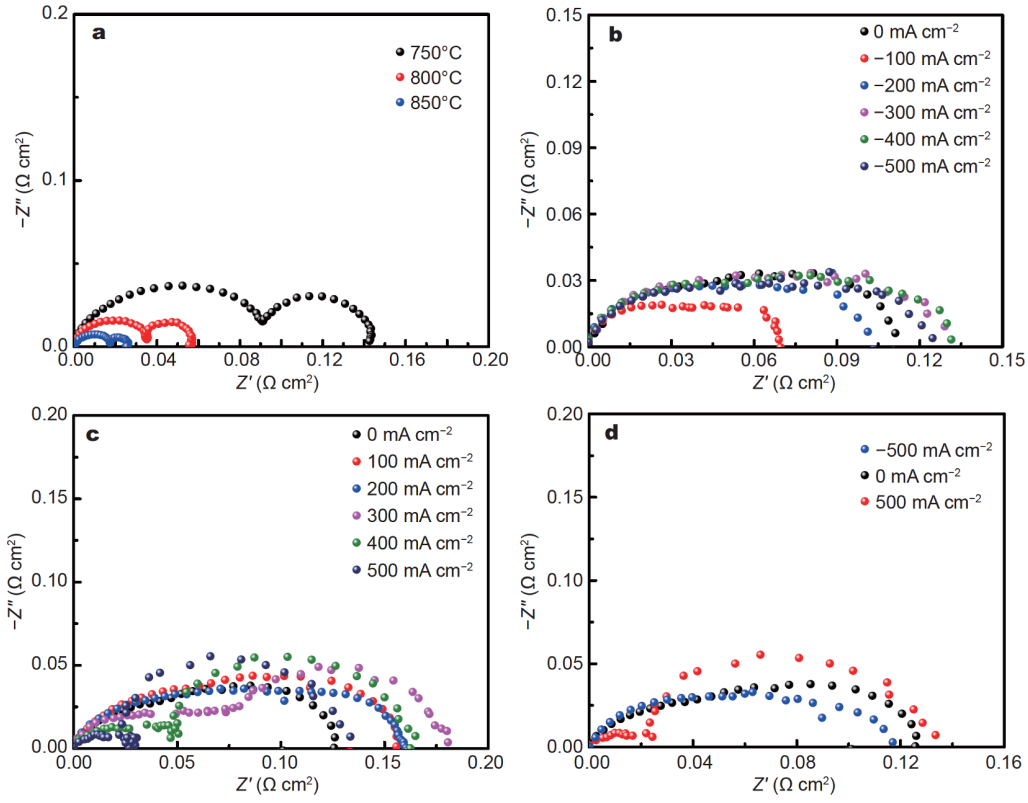

Figure 3 Nyquist plots of the LCaFN electrode under (a) OCV conditions, (b) ORR (cathodic polarization), (c) OER (anodic polarization), and (d) R_p under different current densities at 800°C.

different temperatures is shown in Fig. S6. LCaFN has the lowest R_p and activation energy [27], indicating that LCaFN has high electrocatalytic activity.

Electrochemical performance in SOFC mode

The current density-voltage-power density (*I-V-P*) curves of the Ni-YSZ/YSZ/GDC/LCaFN-GDC full cell at 750–850°C are shown in Fig. 4a. High OCV values indicate a dense electrolyte and leak-proof sealing. The maximum power density (MPD) of the cell increases with temperature and is approximately 1.1 W cm^{-2} at 800°C, while the MPD of the cell with the LSCoF electrode is only 0.95 W cm^{-2} [26,38]. In addition, this value is much higher than the reported results for $NdBaMn_2O_{5+\delta}$, $Co_{1.5}$-$Mn_{1.5}O_4$/$Ce_{0.8}Sm_{0.2}O_{1.9}$, $(La_{0.75}Sr_{0.25})_{0.95}MnO_{3-\delta}$/YSZ, $BaCo_{0.4}Fe_{0.4}Zr_{0.1}Y_{0.1}O_{2.95-\delta}F_{0.05}$, $La_{0.8}Sr_{0.2}MnO_{3-\delta}$, $MnCr_2O_4$/$Gd_{0.1}Ce_{0.9}O_{2-\delta}$, $La_{0.6}Sr_{0.2}Fe_{0.9}Nb_{0.1}O_{3-\delta}$, $La_{0.6}Sr_{0.4}Co_{0.2}Fe_{0.8}$-$O_{3-\delta}$, $La_{0.6}Sr_{0.4}Co_{0.2}Fe_{0.8}O_{3-\delta}$/YSZ, and $NdBa_{0.5}Ca_{0.5}Co_{1.5}$-$Fe_{0.5}O_{5+\delta}$/$Gd_{0.1}Ce_{0.9}O_{2-\delta}$ [39–48], as shown in Fig. 4c. The corresponding EIS are measured as shown in Fig. 4b. The R_p value of the cell with the LCaFN electrode is as low as 0.235 Ω cm^2 at 800°C. With the increasing temperature, both the ohmic resistance and R_p decrease. These results indicate that the full cell with LCaFN as the air electrode has superior electrochemical performance in the SOFC mode.

Electrochemical performance in SOEC mode

Fig. 5a shows the *I-V* curves of the cell with the LCaFN air electrode under different humidities at 800°C. It can be observed that the electrolysis current density increases with increasing humidity. The current density can reach 1.18 A cm^{-2} under 1.3 V at 800°C and 70% absolute humidity (AH). It is noted that a higher electrolysis voltage will result in the appearance of concentration polarization under low-humidity conditions. With increasing humidity, the concentration polarization at high voltage is gradually alleviated. Fig. 5b shows the EIS of the full cell under the corresponding conditions. The ohmic resistance of the cell tends to rise with increasing humidity, which may be due to the oxidation of Ni in the fuel electrode at high temperature and humidity. Therefore,

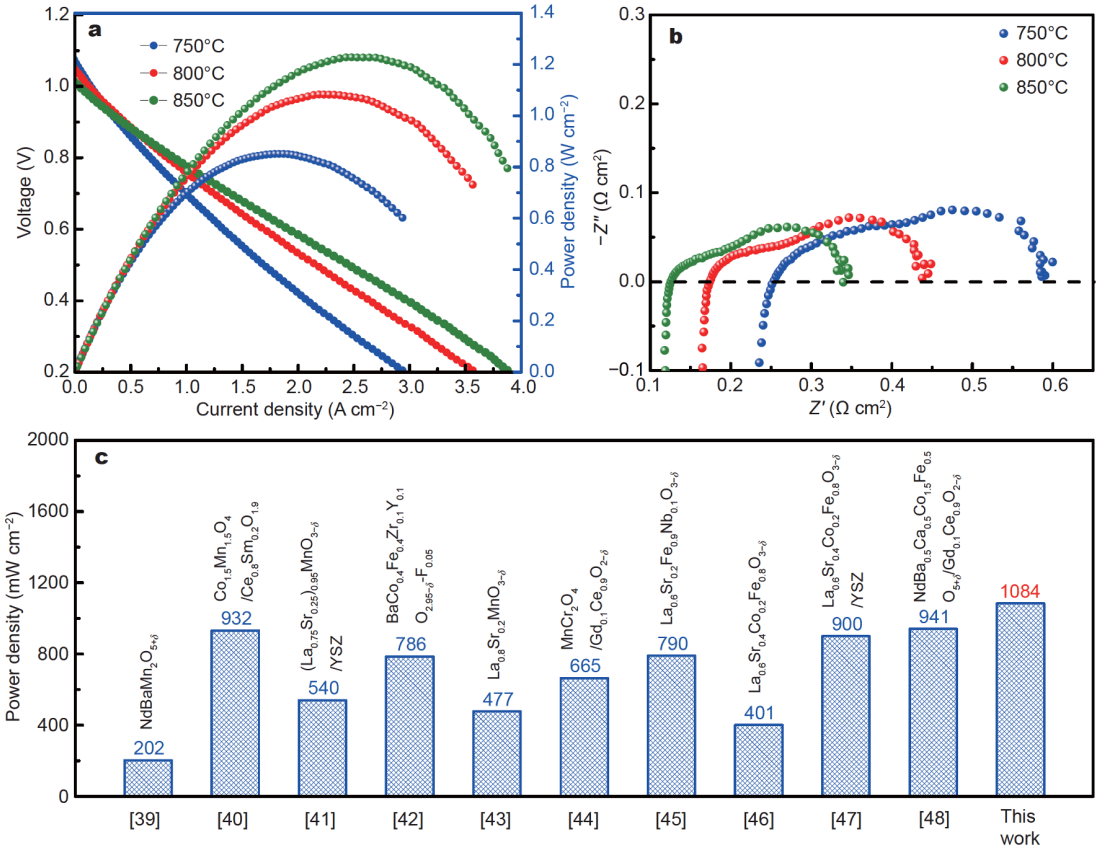

Figure 4 (a) The *I-V-P* curves and (b) corresponding EIS of the Ni-YSZ/YSZ/GDC/LCaFN-GDC cell in wet H_2 at different temperatures. (c) Comparison of the MPD of the LCaFN cell with the reported electrodes.

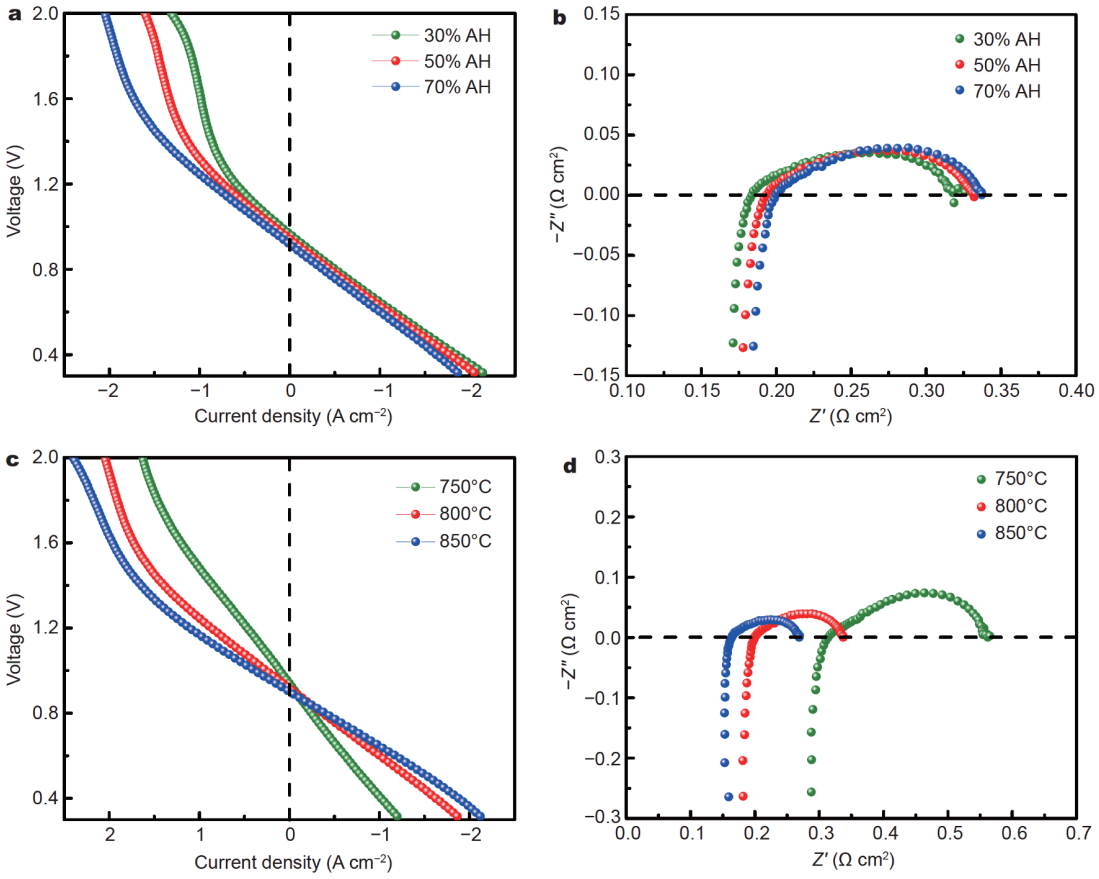

Figure 5 (a) *I-V* curves and (b) EIS of the Ni-YSZ/YSZ/GDC/LCaFN-GDC cell at 800°C with different humidities. (c) *I-V* curves and (d) EIS with 70% AH at different temperatures.

the humidity is maintained at 70% in all subsequent tests. The current density at 1.3 V increases from 0.64 A cm^{-2} at 750°C to 1.39 A cm^{-2} at 850°C, as shown in Fig. 5c. Moreover, with a rise in operating temperature and applied voltage, the slope of the *I-V* curve also increases, which may be related to the concentration polarization. It is clear that both the ohmic resistance and R_p of the cell decrease with increasing temperature, as shown in Fig. 5d. The cell's R_p value is only 0.16 Ω cm^2 at 800°C. Moreover, this cell possesses a high hydrogen production rate as shown in Fig. S7. In addition, the transition near the OCV is smooth in the *I-V* curve, which signifies that the LCaFN-based cell has good reversibility.

Reversibility and stability of RSOCs

To gain better insights into the reversibility of LCaFN-based RSOCs, EIS tests were performed in OCV, SOFC mode (−0.4 A cm^{-2}), and SOEC mode (0.4 A cm^{-2}), as shown in Fig. 6a. The corresponding R_p values of the LCaFN cell are 0.137, 0.139, and 0.146 Ω cm^2, respectively. The close-range values signify and reconfirm the excellent reversibility. The ORR performance of the cell is better than the OER performance because the R_p values in SOFC mode are slightly lower than those in SOEC mode. This result is consistent with the conclusion for the half-cell measurement. The EIS of the cell under different polarization current densities in SOEC mode were further studied, as shown in Fig. 6b. There is no noticeable change in ohmic resistance and R_p. The distribution of relaxation time (DRT) method was used to analyze the impedance spectrum [49]. Within the test frequency range of the EIS, there are five prominent peaks, as shown in Fig. 6c. Each peak represents a different electrochemical reaction process, and its peak area represents the resistance of the corresponding process. Five peaks are distributed in descending order of frequencies. P1, P2 and P4 are related to the processes of ion migration, electron transfer, and gas diffusion of the hydrogen electrode, respectively. P3 represents the oxygen surface exchange process and the oxygen electrode overall dif-

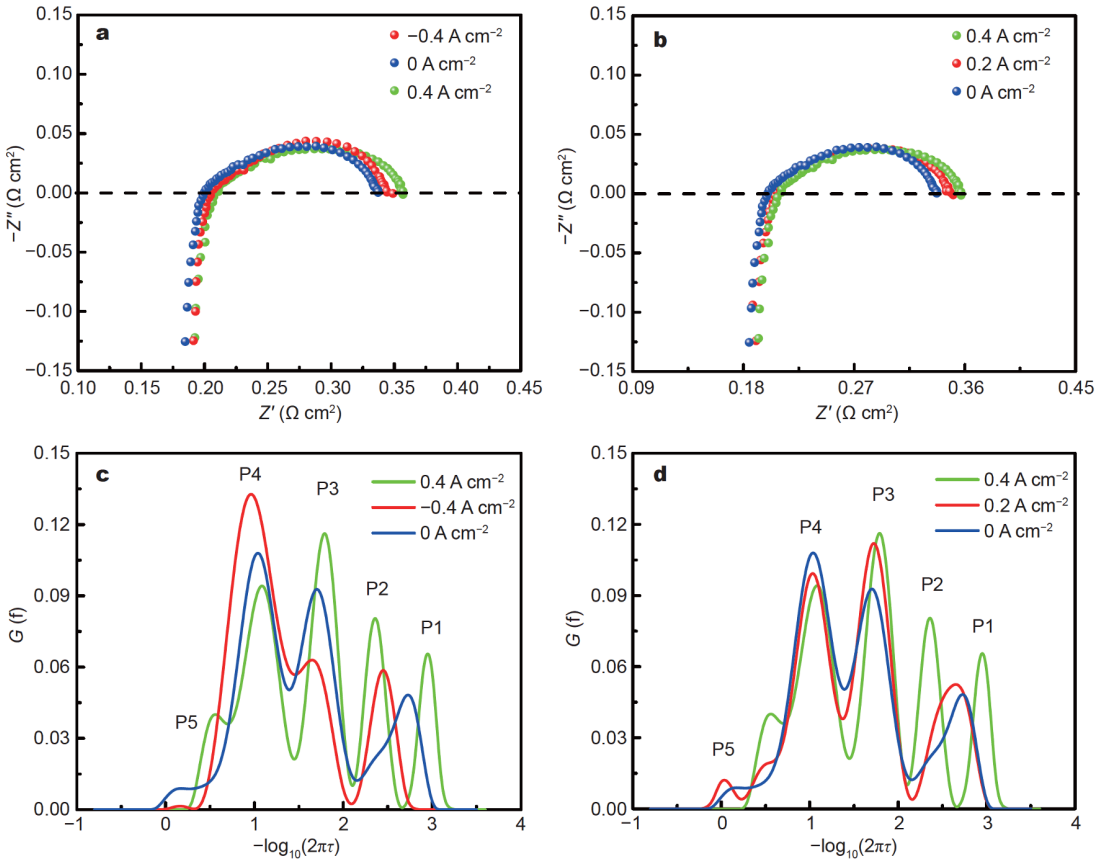

Figure 6 (a, c) Nyquist plots and DRT curves of RSOCs in different working modes and (b, d) different current densities in SOEC mode.

fusion. P5 represents the gas diffusion in the air electrode [50]. P3 and P5 are significantly reduced in the fuel-cell mode due to the ORR process, whereas in SOEC mode, P4 is slightly diminished because of the electrolysis reaction occurring with steam diffusion. Although the variation in R_p values in the SOFC and SOEC modes is insignificant, keen observation of DRT spectra reveals peaks in different modes. This implies that the OER activity of the LCaFN electrode is lower than the ORR activity, which agrees with the previous results. As shown in Fig. 6d, minor changes in the DRT plots at different current densities in the SOEC mode confirm the stability of the cell.

As shown in Fig. 7a, the stability of the LCaFN air electrode at 800°C with electrolysis current densities of 0.4 A cm^{-2} (SOEC mode) and −0.4 A cm^{-2} (SOFC mode) was evaluated. There is no observed degradation during a continuous 12-h test, proving the consistently excellent and stable performance. Fig. 7b shows the cell microstructural characteristics after the test. The cell contained a dense YSZ electrolyte, tight GDC buffer layer and porous LCaFN-GDC electrode. The different cell components are intimately coupled without any noticeable delamination or exfoliation. For the LCaFN-GDC electrode, the loose and porous structure can facilitate the transmission and diffusion of the reaction gas (Fig. 7c). Moreover, the fine particles are beneficial to improving the electrode's electrocatalytic activity.

CONCLUSION

A comparative study of the physicochemical and electrochemical properties of Sr-Co-free perovskite oxide LCaFN with LSFN and LSCoF is performed. The R_p values of the LCaFN electrode are 0.14, 0.06, and 0.03 Ω cm^2 at 750, 800, and 850°C, respectively. The cell with LCaFN displays excellent performance in both SOFC and SOEC modes. In SOFC mode, the MPD of 1.1 W cm^{-2} can be achieved at 800°C. In SOEC mode, the electrolysis current density can reach up to 1.2 A cm^{-2} under 1.3 V with 70% AH at 800°C. Moreover, the cell exhibited good reversibility and stability. Both the electrochemical performance and microstructure remained

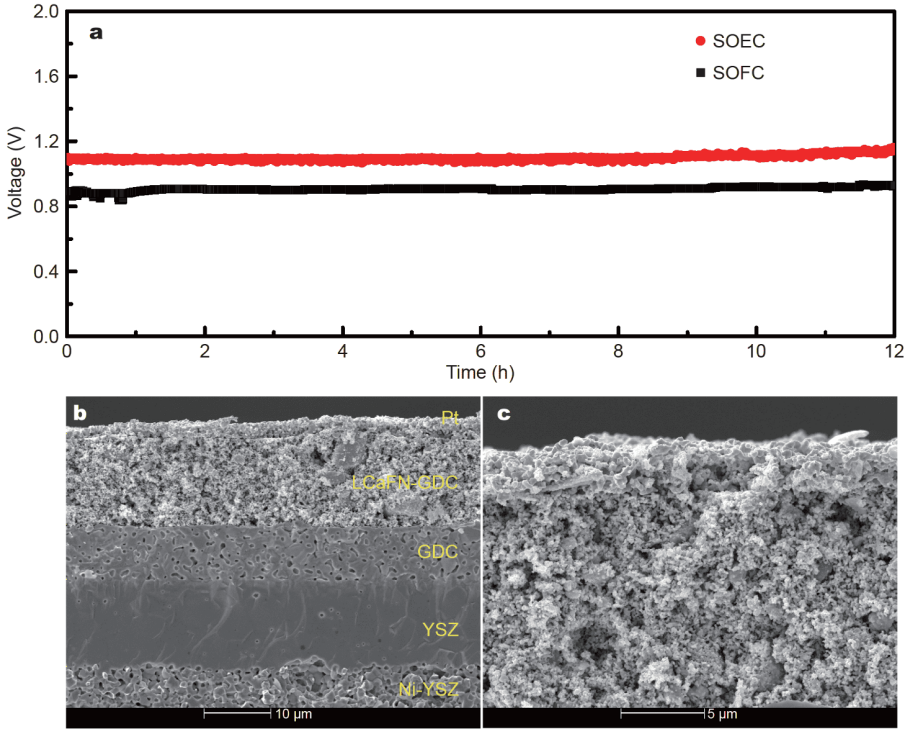

Figure 7 (a) Stability test in both independent modes. (b) Microstructure of the Ni-YSZ/YSZ/GDC/LCaFN-GDC cell after the test. (c) Morphology of the air electrode.

stable even after the 12-h continuous test. The proposed air electrode displays admirable performance in dual modes. Therefore, it is evident that Sr-Co-free perovskite oxide is an ideal candidate material for RSOC air electrodes.

Received 20 August 2020; accepted 18 November 2020; published online 26 January 2021

1 Duan C, Kee R, Zhu H, *et al.* Highly efficient reversible protonic ceramic electrochemical cells for power generation and fuel production. Nat Energy, 2019, 4: 230–240
2 Zheng Y, Wang J, Yu B, *et al.* A review of high temperature co-electrolysis of H_2O and CO_2 to produce sustainable fuels using solid oxide electrolysis cells (SOECs): Advanced materials and technology. Chem Soc Rev, 2017, 46: 1427–1463
3 Choi S, Davenport TC, Haile SM. Protonic ceramic electrochemical cells for hydrogen production and electricity generation: Exceptional reversibility, stability, and demonstrated faradaic efficiency. Energy Environ Sci, 2019, 12: 206–215
4 Graves C, Ebbesen SD, Jensen SH, *et al.* Eliminating degradation in solid oxide electrochemical cells by reversible operation. Nat Mater, 2015, 14: 239–244
5 Ai N, Li N, He S, *et al.* Highly active and stable $Er_{0.4}Bi_{1.6}O_3$ decorated $La_{0.76}Sr_{0.19}MnO_{3+\delta}$ nanostructured oxygen electrodes for reversible solid oxide cells. J Mater Chem A, 2017, 5: 12149–12157
6 Shimada H, Fujimaki Y, Fujishiro Y. Highly active and durable $La_{0.4}Sr_{0.6}MnO_{3-\delta}$ and $Ce_{0.8}Gd_{0.2}O_{1.9}$ nanocomposite electrode for high-temperature reversible solid oxide electrochemical cells. Ceramics Int, 2020, 46: 19617–19623
7 Aguadero A, Pérez-Coll D, Alonso JA, *et al.* A new family of Mo-doped $SrCoO_{3-\delta}$ perovskites for application in reversible solid state electrochemical cells. Chem Mater, 2012, 24: 2655–2663
8 Hong WT, Risch M, Stoerzinger KA, *et al.* Toward the rational design of non-precious transition metal oxides for oxygen electrocatalysis. Energy Environ Sci, 2015, 8: 1404–1427
9 Guan F, Zhang X, Song Y, *et al.* Effect of $Gd_{0.2}Ce_{0.8}O_{1.9}$ nanoparticles on the oxygen evolution reaction of $La_{0.6}Sr_{0.4}Co_{0.2}Fe_{0.8}O_{3-\delta}$ anode in solid oxide electrolysis cell. Chin J Catal, 2018, 39: 1484–1492
10 Tan Y, Duan N, Wang A, *et al.* Performance enhancement of solution impregnated nanostructured $La_{0.8}Sr_{0.2}Co_{0.8}Ni_{0.2}O_{3-\delta}$ oxygen electrode for intermediate temperature solid oxide electrolysis cells. J Power Sources, 2016, 305: 168–174
11 López-Robledo MJ, Laguna-Bercero MA, Larrea A, *et al.* Reversible operation of microtubular solid oxide cells using $La_{0.6}Sr_{0.4}Co_{0.2}Fe_{0.8}O_{3-\delta}$-$Ce_{0.9}Gd_{0.1}O_{2-\delta}$ oxygen electrodes. J Power Sources, 2018, 378: 184–189
12 Fu Y-P, Subardi A, Hsieh M-Y, *et al.* Electrochemical properties of $La_{0.5}Sr_{0.5}Co_{0.8}M_{0.2}O_{3-\delta}$ (M = Mn, Fe, Ni, Cu) perovskite cathodes for IT-SOFCs. J Am Ceram Soc, 2016, 99: 1345–1352
13 Majnoni d'Intignano X, Cademartori D, Clematis D, *et al.* Infiltrated $Ba_{0.5}Sr_{0.5}Co_{0.8}Fe_{0.2}O_{3-\delta}$-based electrodes as anodes in solid oxide electrolysis cells. Energies, 2020, 13: 3659
14 Zhu L, Wei B, Wang Z, *et al.* Electrochemically driven deactivation and recovery in $PrBaCo_2O_{5+\delta}$ oxygen electrodes for reversible solid oxide fuel cells. ChemSusChem, 2016, 9: 2443–2450

15 Ebbesen SD, Jensen SH, Hauch A, *et al.* High temperature electrolysis in alkaline cells, solid proton conducting cells, and solid oxide cells. Chem Rev, 2014, 114: 10697–10734
16 Laguna-Bercero MA. Recent advances in high temperature electrolysis using solid oxide fuel cells: A review. J Power Sources, 2012, 203: 4–16
17 Zhou Q, Cheng Y, Li W, *et al.* Investigation of cobalt-free perovskite $Sr_2FeTi_{0.75}Mo_{0.25}O_{6-\delta}$ as new cathode for solid oxide fuel cells. Mater Res Bull, 2016, 74: 129–133
18 Tian Y, Zhang L, Jia L, *et al.* Novel quasi-symmetrical solid oxide electrolysis cells with *in-situ* exsolved cathode for CO_2 electrolysis. J CO_2 Util, 2019, 31: 43–50
19 Bian LZ, Wang LJ, Chen N, *et al.* Enhanced performance of $La_{0.7}Sr_{0.3}Fe_{0.9}Ni_{0.1}O_3$ cathode by partial substitution with Ce. Ceramics Int, 2017, 43: 982–987
20 Tian Y, Zhang L, Liu Y, *et al.* A self-recovering robust electrode for highly efficient CO_2 electrolysis in symmetrical solid oxide electrolysis cells. J Mater Chem A, 2019, 7: 6395–6400
21 Tian Y, Zheng H, Zhang L, *et al.* Direct electrolysis of CO_2 in symmetrical solid oxide electrolysis cell based on $La_{0.6}Sr_{0.4}Fe_{0.8}Ni_{0.2}O_{3-\delta}$ electrode. J Electrochem Soc, 2018, 165: F17–F23
22 Meng L, Wang F, Wang A, *et al.* High performance $La_{0.8}Sr_{0.2}MnO_3$-coated $Ba_{0.5}Sr_{0.5}Co_{0.8}Fe_{0.2}O_3$ cathode prepared by a novel solid-solution method for intermediate temperature solid oxide fuel cells. Chin J Catal, 2014, 35: 38–42
23 Sumi H, Ohshiro T, Nakayama M, *et al.* Prevention of reaction between (Ba,Sr)(Co,Fe)O_3 cathodes and yttria-stabilized zirconica electrolytes for intermediate-temperature solid oxide fuel cells. Electrochim Acta, 2015, 184: 403–409
24 Konysheva E, Penkalla H, Wessel E, *et al.* Chromium poisoning of perovskite cathodes by the ODS alloy $Cr_5Fe_1Y_2O_3$ and the high chromium ferritic steel Crofer22APU. J Electrochem Soc, 2006, 153: A765
25 Kim YM, Chen X, Jiang SP, *et al.* Effect of strontium content on chromium deposition and poisoning in $Ba_{1-x}Sr_xCo_{0.8}Fe_{0.2}O_{3-\delta}$ ($0.3 \le x \le 0.7$) cathodes of solid oxide fuel cells. J Electrochem Soc, 2011, 159: B185–B194
26 Tian Y, Wang W, Liu Y, *et al.* Cobalt-free perovskite oxide $La_{0.6}Sr_{0.4}Fe_{0.8}Ni_{0.2}O_{3-\delta}$ as active and robust oxygen electrode for reversible solid oxide cells. ACS Appl Energy Mater, 2019, 2: 3297–3305
27 Muhammed Ali SA, Anwar M, Somalu MR, *et al.* Enhancement of the interfacial polarization resistance of $La_{0.6}Sr_{0.4}Co_{0.2}Fe_{0.8}O_{3-\delta}$ cathode by microwave-assisted combustion method. Ceramics Int, 2017, 43: 4647–4654
28 Stevenson JW, Armstrong TR, Carneim RD, *et al.* Electrochemical properties of mixed conducting perovskites $La_{1-x}M_xCo_{1-y}Fe_yO_{3-\delta}$ (M = Sr, Ba, Ca). J Electrochem Soc, 1996, 143: 2722–2729
29 Huheey JE, Keiter EA, Keiter RL. Inorganic Chemistry: Principles of Structure and Reactivity. New York: Harper Collins, 1993
30 Whangbo MH, Koo HJ, Villesuzanne A, *et al.* Effect of metal-oxygen covalent bonding on the competition between jahn-teller distortion and charge disproportionation in the perovskites of high-spin d^4 metal ions $LaMnO_3$ and $CaFeO_3$. Inorg Chem, 2002, 41: 1920–1929
31 Swierczek K. Thermoanalysis, nonstoichiometry and thermal expansion of $La_{0.4}Sr_{0.6}Co_{0.2}Fe_{0.8}O_{3-\delta}$, $La_{0.2}Sr_{0.8}Co_{0.2}Fe_{0.8}O_{3-\delta}$, $La_{0.9}Sr_{0.1}Co_{1/3}Fe_{1/3}Ni_{1/3}O_{3-\delta}$ and $La_{0.6}Sr_{0.4}Co_{0.2}Fe_{0.6}Ni_{0.2}O_{3-\delta}$ perovskites. Solid State Ion, 2008, 179: 126–130
32 Hayashi H, Kanoh M, Quan CJ, *et al.* Thermal expansion of Gd-doped ceria and reduced ceria. Solid State Ion, 2000, 132: 227–233
33 Yang E, Noh Y, Ramesh S, *et al.* The effect of promoters in $La_{0.9}M_{0.1}Ni_{0.5}Fe_{0.5}O_3$ (M = Sr, Ca) perovskite catalysts on dry reforming of methane. Fuel Process Technol, 2015, 134: 404–413
34 Sun YF, Li JH, Cui L, *et al.* A-site-deficiency facilitated *in situ* growth of bimetallic Ni-Fe nano-alloys: A novel coking-tolerant fuel cell anode catalyst. Nanoscale, 2015, 7: 11173–11181
35 Natile MM, Poletto F, Galenda A, *et al.* $La_{0.6}Sr_{0.4}Co_{1-y}Fe_yO_{3-\delta}$ perovskites: Influence of the Co/Fe atomic ratio on properties and catalytic activity toward alcohol steam-reforming. Chem Mater, 2008, 20: 2314–2327
36 Huang TJ, Shen XD, Chou CL. Characterization of Cu, Ag and Pt added $La_{0.6}Sr_{0.4}Co_{0.2}Fe_{0.8}O_{3-\delta}$ and gadolinia-doped ceria as solid oxide fuel cell electrodes by temperature-programmed techniques. J Power Sources, 2009, 187: 348–355
37 Zhou F, Zhou L, Hu M, *et al.* Pd-doped $La_{0.6}Sr_{0.4}Co_{0.2}Fe_{0.8}O_{3-\delta}$ perovskite oxides as cathodes for intermediate temperature solid oxide fuel cells. Solid State Ion, 2018, 319: 22–27
38 Liu J, Barnett SA. Thin yttrium-stabilized zirconia electrolyte solid oxide fuel cells by centrifugal casting. J Am Ceramic Soc, 2004, 85: 3096–3098
39 Abdalla AM, Hossain S, Zhou J, *et al.* $NdBaMn_2O_{5+\delta}$ layered perovskite as an active cathode material for solid oxide fuel cells. Ceramics Int, 2017, 43: 15932–15938
40 Zhang L, Li D, Zhang S. One-step synthesized $Co_{1.5}Mn_{1.5}O_4$-$Ce_{0.8}Sm_{0.2}O_{1.9}$ composite cathode material for intermediate temperature solid oxide fuel cells. Ceramics Int, 2017, 43: 2859–2863
41 Wang JX, Sun JL, He CR, *et al.* Mass synthesis of high performance $(La_{0.75}Sr_{0.25})_{0.95}MnO_{3\pm\delta}$ nano-powder prepared *via* a low-carbon chemical solution method. J Power Sources, 2014, 253: 424–430
42 Wang W, Zhang X, Zhang D, *et al.* Highly promoted performance of triple-conducting cathode for YSZ-based SOFC *via* fluorine anion doping. Ceramics Int, 2020, 46: 23964–23971
43 Salehzadeh D, Torabi M, Sadeghian Z, *et al.* A multiscale-architecture solid oxide fuel cell fabricated by electrophoretic deposition technique. J Alloys Compd, 2020, 830: 154654
44 Li P, Duan N, Ma J, *et al.* Exploring $MnCr_2O_4$–$Gd_{0.1}Ce_{0.9}O_{2-\delta}$ as a composite electrode material for solid oxide fuel cell. Int J Hydrogen Energy, 2019, 44: 31333–31341
45 Guan C, Wang Y, Chen K, *et al.* Molten salt synthesis of Nb-doped (La, Sr)FeO_3 as the oxygen electrode for reversible solid oxide cells. Mater Lett, 2019, 245: 114–117
46 Fan H, Keane M, Singh P, *et al.* Electrochemical performance and stability of lanthanum strontium cobalt ferrite oxygen electrode with gadolinia doped ceria barrier layer for reversible solid oxide fuel cell. J Power Sources, 2014, 268: 634–639
47 Fan H, Keane M, Li N, *et al.* Electrochemical stability of $La_{0.6}Sr_{0.4}Co_{0.2}Fe_{0.8}O_{3-\delta}$-infiltrated YSZ oxygen electrode for reversible solid oxide fuel cells. Int J Hydrogen Energ, 2014, 39: 14071–14078
48 Tian Y, Liu Y, Wang W, *et al.* High performance and stability of double perovskite-type oxide $NdBa_{0.5}Ca_{0.5}Co_{1.5}Fe_{0.5}O_{5+\delta}$ as an oxygen electrode for reversible solid oxide electrochemical cell. J Energy Chem, 2020, 43: 108–115
49 Kobayashi K, Suzuki TS. Distribution of relaxation time analysis for non-ideal immittance spectrum: Discussion and progress. J Phys Soc Jpn, 2018, 87: 094002
50 Yan J, Chen H, Dogdibegovic E, *et al.* High-efficiency intermediate temperature solid oxide electrolyzer cells for the conversion of carbon dioxide to fuels. J Power Sources, 2014, 252: 79–84

Acknowledgements This work was supported by the National Key Research & Development Program of China (2020YFB1506304, 2017YFE0129300 and 2016YFE0126900), the National Natural Science Foundation of China (52072135, 51672095 and U1910209), and the Major Science and Technology Innovation Project of Hubei Province (2018AAA057). Analytical and Testing Centre of Huazhong University of Science and Technology is appreciated for sample characterization assistance.

Author contributions Wang W conducted the experiments and wrote this paper; Tian Y gave the overall concept and revised the draft; Abhishek N conducted the data analysis; Liu Y and Li Y contributed to the theoretical analysis; Chi B was responsible for review and editing; Pu J contributed to resource support. All authors participated in the general discussion.

Conflict of interest The authors declare that they have no conflict of interest.

Supplementary information Supporting data are available in the online version of the paper.

Wenjie Wang received her Bachelor degree in engineering from China University of Geosciences (Wuhan). She is currently studying for a Master's degree under the supervision of Professor Bo Chi at Huazhong University of Science and Technology (HUST). Her research interests include electrode materials for electrochemical energy storage devices, such as fuel cells.

Yunfeng Tian is currently a lecturer in the School of Materials Science and Physics at China University of Mining and Technology. He received his PhD degree from HUST, under the supervision of Professor Bo Chi. His research focuses on the development and characterization of novel electrode materials for solid oxide fuel cells and electrolysis cells.

Bo Chi is a professor of the Center for Fuel Cell Innovation, School of Materials Science and Technology at HUST, China. He received his BSc and Master degrees in materials science from China University of Geosciences (Wuhan) in 1998 and 2001, respectively, and his PhD degree in materials science from Tsinghua University in 2005. He worked as JSPS (The Japan Society for the Promotion of Science) postdoc at the National Institute of Advanced Industrial Science and Technology (AIST), Japan from 2005 to 2007 before he joined HUST. His current research interests are solid oxide fuel cells/electrolysis cells, metal-air battery and solar cells.

制备无锶无钴的钙钛矿氧化物作为高性能可逆固体氧化物电池的空气电极

王文洁[1], 田云峰[1*], 刘云[2], Nalluri Abhishek[1], 李宜桐[1], 池波[1,3*], 蒲健[1,3]

摘要 可逆固体氧化物燃料电池(RSOC)是一种新型高效的能量存储和转化装置，具有高效率、无污染和模块化等优点. 在本文中, $La_{0.6}Ca_{0.4}Fe_{0.8}Ni_{0.2}O_{3-\delta}$ (LCaFN)被用于高性能RSOC的无锶无钴钙钛矿空气电极. 与$La_{0.6}Sr_{0.4}Fe_{0.8}Ni_{0.2}O_{3-\delta}$ (LSFN)和$La_{0.6}Sr_{0.4}Co_{0.2}Fe_{0.8}O_{3-\delta}$ (LSCoF)相比，LCaFN具有较高的导电性(297 S cm^{-1})、良好的热膨胀系数兼容性(11.2×10^{-6} K^{-1})和较高的化学稳定性. 此外，LCaFN在800°C还具有高催化活性和低极化电阻(0.06 Ω cm^2). 单电池Ni-YSZ/YSZ/GDC/LCaFN-GDC在800°C下的最大功率密度为1.08 W cm^{-2}. 在固体氧化物电解池模式下, 电池在800°C、70% H_2O、1.3 V电压下可实现约1.2 A cm^{-2}的电流密度. 同时电池还表现出良好的可逆性和运行稳定性. 研究结果表明，LCaFN作为RSOC的空气电极材料具有广阔的应用前景.

